applied sciences

MDPI

Article

Experiments on the State Boundary Surface of Aeolian Sand for Road Building in the Tengger Desert

Zhigang Ma [1,2] and Xuefeng Li [1,2,*]

1 School of Physics and Electronic-Electrical Engineering, Ningxia University, Yinchuan 750021, China
2 Solid Mechanics Institute, Ningxia University, Yinchuan 750021, China
* Correspondence: lixuefeng1928@163.com

Abstract: As a special road-building material widely distributed in desert areas, critical state soil mechanics is used to study the mechanical properties of sand and make up for the lack of research on its engineering characteristics. A series of drained and undrained triaxial compression tests with a loading rate of 0.12 mm/min medium-density aeolian sands taken from Tengger Desert in the northwest of China was carried out to obtain the three-dimensional state boundary surface. The test results reveal that the strength gained from drained and undrained tests increased, respectively, linearly and non-linearly with the increase of the effective confining pressure. Affected by the variation of pore pressure and shear rate, the undrained strength was higher than the drained strength at low effective confining pressures, and the two types of strengths tend to be consistent when the effective confining pressure becomes greater than 800 kPa. The volumetric changes of the aeolian specimens transition from dilatation to contraction when the effective confining pressures increase. The investigation of the strength, deformation and failure characteristics gives rise to the shape parameters of its state boundary surface, which provides not only a basis for the constitutive modelling of the aeolian sand, but also a reference for roadbed construction and other foundation engineering in desert areas.

Keywords: aeolian sand; triaxial test; state boundary surface; strength characteristics; deformation

check for updates

Citation: Ma, Z.; Li, X. Experiments on the State Boundary Surface of Aeolian Sand for Road Building in the Tengger Desert. *Appl. Sci.* **2023**, *13*, 879. https://doi.org/10.3390/app13020879

Academic Editors: Jue Li, Junhui Zhang, Junfeng Gao, Junhui Peng and Wensheng Wang

Received: 20 December 2022
Revised: 6 January 2023
Accepted: 6 January 2023
Published: 9 January 2023

1. Introduction

The state boundary surface is the unique physical state relationship formed by effective stress paths of soil in a three-dimensional space composed of generalized normal stress, shear stress and specific volume, and it provides an outer limit to the combinations of effective stress and specific volume which the soil can reach [1]. In road building, it can predict the limit state of aeolian sand subgrade failure. The state boundary surface is the basis of critical state soil mechanics and is crucial in studies of the soil mechanical properties, which have been widely used to study the mechanical behaviors of remodeled clay. Aeolian sand is a special material for roadbed filling, which is widely distributed in desert areas, while there are only a few basic experiments for engineering applications. Moreover, the basic experimental results related to critical states are rather scarce. In recent years, much infrastructure, such as highways, railways, transmission lines and other projects, has been built in desert areas. In addition, the numerical simulation of the dynamic response of multi-layer pavement under a moving load is gradually enriched [2,3]. However, the lack of research on the mechanical properties of aeolian sand has seriously restricted the geotechnical application in desert areas. Therefore, experimental characteristics of the state boundary surface of aeolian sand is urgently required for a better understanding the mechanical behaviour of this material.

Currently, most of the existing research on aeolian sands focuses on their engineering aspects, such as particle-size distribution, compaction characteristics, bearing capacity, shear resistance and proportioned concrete [4–6]. The particle-size distribution of aeolian sand in several regions was analysed by different researchers, for instance, Li et al. [7] for the Tengger Desert, Liu et al. [8] for the Mu Us Desert, Ning et al. [9], Guo et al. [10] for the Badain Jaran Desert, Zhang et al. [11] for the Qinghai Lake East Sandy Land, etc. These studies provide rich references for the construction of a foundation treatment in desert areas. Other researchers, e.g., Yuan et al. [12], Li et al. [13], Yin et al. [14], studied the compaction characteristics of aeolian sand. Du et al. [15], Yu et al. [16], Yi et al. [17] and Zheng et al. [18] studied the shear strength characteristics in different desert regions. Yin et al. [19] and Li et al. [20] studied the bearing capacity characteristics of aeolian sand foundations. Although the existing research has accumulated valuable engineering experience for foundation construction in desert areas, a systematic and in-depth triaxial test study is needed to better obtain the unique characteristics of its physical state.

So far aeolian sand has been rarely studied in triaxial tests. Some authors have studied the dynamic properties of aeolian sand with dynamic triaxial tests, e.g., Deng [21], Song [22], Liu [23], Song et al. [24], Liu et al. [25], Luo et al. [26] and Bao et al. [27]. Other authors focus on the static strength of sand. For instance, Li et al. [28] studied the strength characteristics of cement-improved aeolian sand; Badanagki [29] obtained the shear strength and stiffness of aeolian sand in the Sahara Desert, Libya, by a series of drained and undrained triaxial tests; Song [24] obtained the strength characteristics of the aeolian sand in the Mu Us Desert, China, at different stress paths, densities and moisture contents; Qureshi et al. [30] obtained the strength and softening resistance of aeolian sand treated by biopolymer in Al-Sharqia desert; Souza et al. [31] determined the critical state parameters of aeolian sand in Natal, Brazil by triaxial tests with different initial densities; Wei et al. [32] obtained the mechanical properties of aeolian sand and fly ash at different proportions. In particular, Li Xuefeng et al. [33–35] studied the characteristics of deformation, strength and failure of aeolian sand in the Tengger Desert, China at different spatial stress states, different densities and multiple confining pressures. All in all, the unique mechanical properties of aeolian sand have attracted increasing popularity, but some other aspects, such as the critical state, phase transformation and dilatancy of aeolian sand at different stress states and stress paths, need to be studied further. In particular, the determination of its state boundary surface is rarely reported.

In this paper, a series of triaxial drained and undrained tests on the medium-density specimens were conducted to obtain the unique relationship of the state boundary surface of the aeolian sand taken from the Tengger Desert in China. The mechanical responses are measured at different confining pressures. The critical state lines, phase transformation lines and dilatancy characteristics are determined. According to the unique relationship between the stress state and the volume state, the state boundary surface in the p-q-e space is established. The test results improve our understanding of the mechanical response and helps to establish a reasonable constitutive relationship for aeolian sand.

2. Test Method

2.1. Test Apparatus

The triaxial apparatus used in the test was produced by Ningxi Soil Apparatus in Nanjing, China, which can be controlled by stress or strain (Figure 1). The triaxial apparatus is mainly composed of a host, a pressure controller, and a multi-channel communication digital acquisition apparatus. The apparatus is controlled by a single chip computer, and each part can work independently. Multi-channel communication can collect and process data in real time. The apparatus can perform various stress path tests and drained or undrained triaxial tests, in which the drained triaxial test can obtain the real strength of the material, and the undrained triaxial test corresponding to the rapid construction can obtain the pore pressure development. The size of the cylindrical specimen is Φ39.1 mm $\times$ 80 mm, the axial load range is 0~30 kN, and its measurement accuracy is $\pm$1%. The range of the confining pressure controller is 0~1.99 MPa, the range of the back pressure controller is 0~0.99 MPa, and the control accuracy is $\pm$0.5%FS (Full Scale).

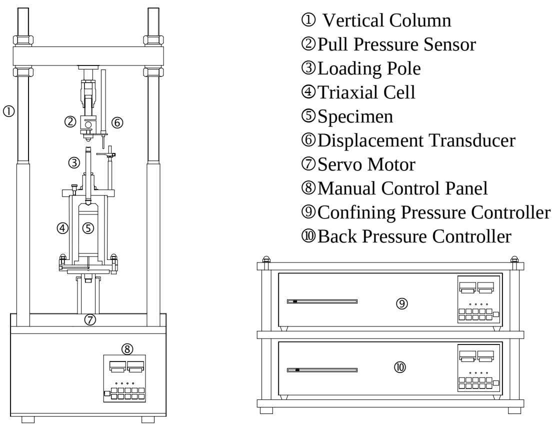

Figure 1. SLB-1 triaxial apparatus, Nanjing, China.

2.2. Test Material

The sand specimen is aeolian sand sampled from the Tengger Desert, China. The Tengger Desert is a typical enrichment area of aeolian sand. Aeolian sand in this area is a special granular material with heterogeneity, cohesionless, uniform particle size, strong permeability and remarkable anisotropy characteristics. The compaction curve has bimodal characteristics, which is also a type of collapsible soil [36]. Therefore, the sand tested in this paper is widely representative. Figure 2 shows the microscopic image of the used sand.

The mass of the aeolian sand with a particle size larger than 0.075 mm exceeds 85% of the total mass. The moisture content of natural aeolian sand is 0.14%; the maximum dry density is 1.68 g/cm^3; the minimum dry density is 1.40 g/cm^3; the specific gravity of sand is 2.67; the maximum void ratio is 0.907, and the minimum void ratio is 0.589. The coefficient of nonuniformity C_u is 1.31, the coefficient of curvature C_c is 2.66, and the fine particle content is less than 5%. According to the "Engineering Classification Standard of Soil" (GB/T 50145-2007), the sand is classified as poorly graded sand. Table 1 shows the particle-size distribution of aeolian sand measured by the sieving method (the data in Table 1 are the average results of three sieving tests). In the table, the sieve mass with a particle size of 0.1~0.25 mm is 750.8 g, accounting for 75.08% of the total mass of the sample, which is the highest particle size of aeolian sand.

Table 1. Particle size gradation of aeolian sand in the Tengger Desert.

Mass of sample taken for fine sieve analysis = 1000 g Sand mass on 2 mm sieve = 0 g Sand mass under 2 mm sieve = 1000 g			The percentage of sand less than 0.075 mm in the total sand mass = 1.23% The percentage of sand less than 2 mm in the total sand mass = 100%	
Particle Size/mm	Cumulative Sand Mass on the Sieve/g	Mass of Sand with Particle Size Smaller than the Aperture/g	The Mass Percentage of Sand with a Particle Size Smaller than the Aperture/%	The Mass Percentage of Total Sand Whose Particle Size Is Smaller than the Aperture /%
0	0	0	0	0
0.075	12.3	12.3	1.23	1.23
0.1	131.3	143.6	13.13	14.36
0.25	750.8	894.4	75.08	89.44
0.5	104.4	998.8	10.44	99.88
1	1.2	1000	0.12	100

2.3. Test Process and Scheme

The specimen preparation process was completed by using a split mould, a rubber membrane and a vacuum pump. The vacuum was used to make the rubber membrane close to the inner wall of the split mould. The multiple sieving pluviation method is used for the specimen preparation. The process of specimen preparation and specimen installation is shown in Figure 3. The relative density D_r is controlled to be 0.5, the dry density ρ_d = 1.53 g/cm^3, and the initial void ratio e_0 = 0.745 (medium density). After the specimen was prepared, it was necessary to vacuum the specimen through an exhaust hole on the top cap of the specimen to ensure the stability of the specimen size. To this end, a negative pressure of 20 kPa inside the specimen was maintained to fix the shape of the specimen. Afterwards, two steps of hydraulic saturation and back pressure saturation were performed to saturate the specimens. After the saturation reaches higher than 95%, the specimen consolidation and triaxial drained and undrained shear test were carried out with reference to ASTM (D7181-11).

Figure 2. Microscopic image of test material (0.5 mm/grid).

Figure 3. Specimen preparation and specimen installation.

To obtain the state boundary surface of the aeolian sand in the three-dimensional space, it is necessary to obtain the effective stress paths and strength and deformation at different confining pressures. For this purpose, the drained and undrained triaxial tests at the confining pressure σ_3 of 50, 100, 200, 400 and 800 kPa were designed. The key control parameters of the test scheme were detailed in Table 2.

Table 2. Triaxial test control parameters.

Material Type	Saturability	Effective Confining Pressure σ_3 (kPa)	Drained Conditions	Strain Loading Rate (mm/min)
Aeolian sand	More than 95%	50 100 200 400 800	I.Drained II.Undrained	0.12

3. Test Results

3.1. Stress-Strain Relationships

Figure 4a,b shows the variation of the generalized shear stress and volumetric strain with axial strain under the drained conditions. Due to the complex and diverse in natural particle shapes of the aeolian sand (Figure 1), the particle internal friction is strong, resulting in obvious nonlinear characteristics in the stress-strain curves. At a low effective confining pressure ($\sigma_3 \leq 100$ kPa), the specimens exhibit strain hardening behaviour, and at a high effective confining pressure, they show strain-softening behaviours. The higher the effective confining pressure, the more obvious the softening characteristic, the greater the elastic modulus, the higher the peak strength, and the longer the elastic-plastic stage. At low effective confining pressure, the aeolian sand first undergoes contraction deformation and then dilates until failure is achieved. Meanwhile, the characteristics of contraction and dilatation are affected significantly by the effective confining pressure. With the increase of the effective confining pressure, the volumetric changes develop from dilatation to contraction. While the effective confining pressure reaches 800 kPa, only the contraction deformation occurs (compared to the initial volume of the specimen).

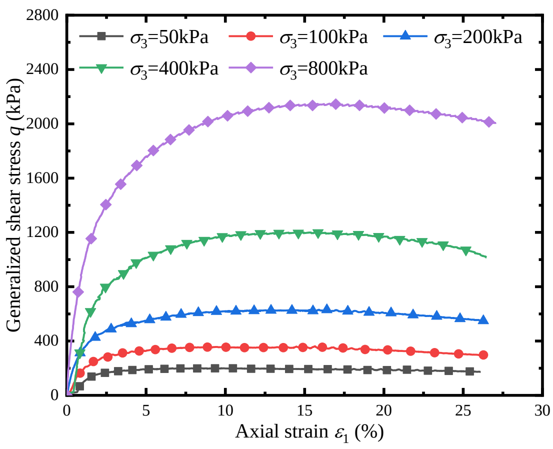

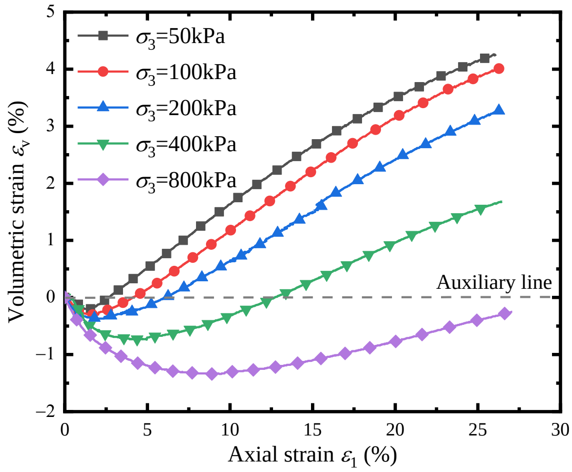

Figure 4. Relationships between stress and volumetric strain with axial strain at drained condition. (**a**) Stress-strain relationships. (**b**) Volumetric strain-strain relationships.

Figure 5a,b show the variation of generalized shear stress and pore pressure with axial strain under undrained conditions. Figure 5a shows that the stress-strain relationships are softened only at relatively low effective confining pressures (e.g., 50, 100 and 200 kPa), and hardened at high effective confining pressures (>200 kPa). A greater effective confining pressure gives rise to a greater elastic modulus and a higher peak strength. Compared with the stress-strain relationships under the drained condition, the peak stress point of the undrained test is higher and the elastic-plastic stage is longer under the same load conditions. The results suggest that the undrained shear rate needs to be reduced to fully dissipate the excess pore pressure. Figure 5b shows the variation of pore pressure, implying that the dilatancy increases gradually with the increase of effective confining pressure. At low effective confining pressure, the negative pore pressure generally increases, while at high effective confining pressure, the pore pressure increases generally. It also shows that only dilation occurs at low effective confining pressure, while only contraction occurs at high effective confining pressure. This is consistent with the results obtained from drained tests. However, pore pressure has a greater influence on the stress-strain relationships under undrained conditions, and aeolian sand is more prone to dilatancy failure.

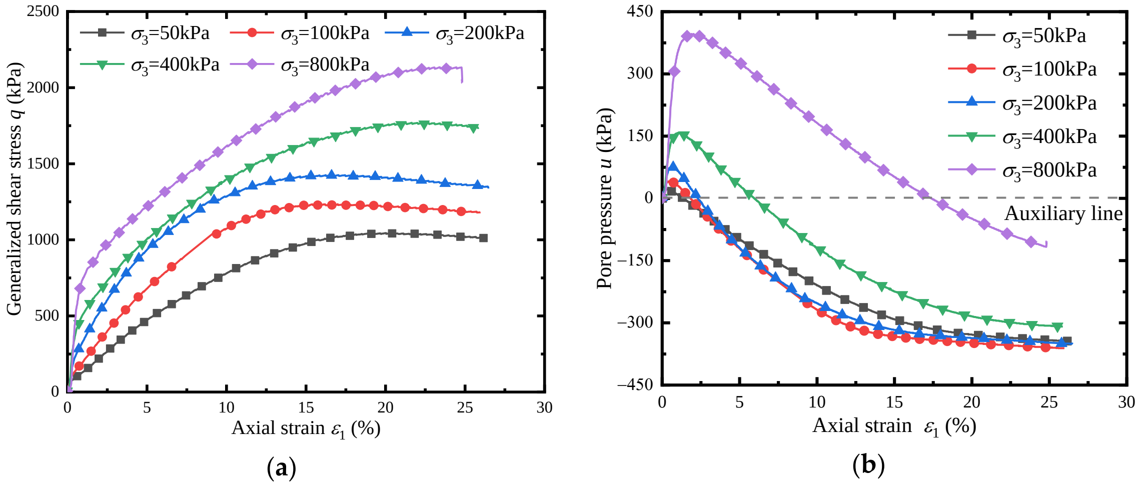

Figure 5. Relationships between stress and pore pressure with axial strain under undrained conditions. (**a**) Stress-strain relationships. (**b**) Pore pressure-strain relationships.

Figure 6 shows the variation of pore pressure coefficient A with axial strain. Skempton [37] reported that the specimen contracts for $A > 0$, and it dilates at $A < 0$. Therefore, in Figure 6, the pore pressure and strain relationships above auxiliary line $A = 0$ are contraction, and below auxiliary line $A = 0$ is dilation. The test results of the pore pressure coefficient A also show that the deformation and failure mode of the aeolian sand is dilatation under undrained conditions, and the contraction part only occurs within 2% of the axial strain.

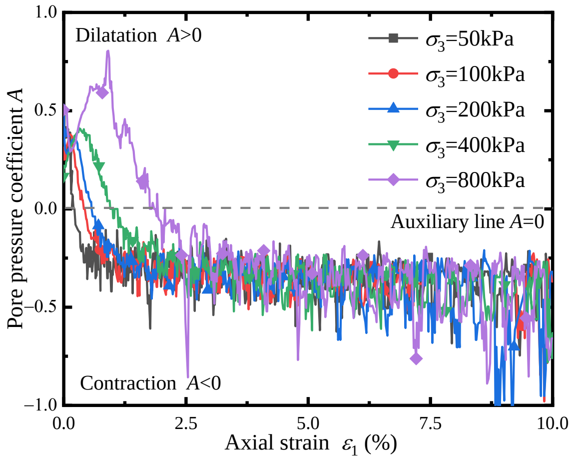

Figure 6. Relationships between pore pressure coefficient and axial strain.

Figure 7a,b shows the relationships between axial strain and radial strain under drained and undrained conditions. The relationships between the axial strain and radial strain change linearly under drained condition. As the effective confining pressure increases, the slope of the linear relationship increases negatively, indicating that the aeolian sand has an initial anisotropy, and the initial anisotropy decreases with the increase of the effective confining pressure continuously. Figure 7b shows that the relationships between the axial strain and radial strain change linearly under undrained conditions, which always satisfies the equation $\varepsilon_1 = -2\varepsilon_3$. The anisotropy characteristic is not obvious, which may be related to the loading rate of the test.

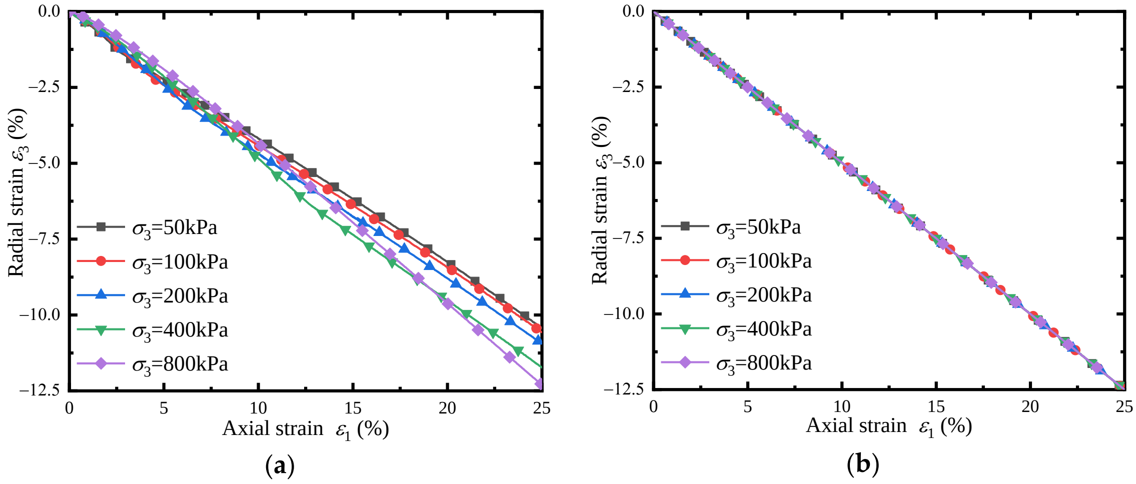

Figure 7. Relationships between axial strain and radial strain. (**a**) Drained. (**b**) Undrained.

Figures 8a,b and 9a,b show the relationships between generalized stress ratio η and generalized shear strain ε_s of aeolian sand and the relationships between ε_s/η and ε_s under drained and undrained conditions, respectively. Comparing Figures 8a and 9a, it can be concluded that the peak stress ratio decreases gradually with the increase of effective confining pressure in both the drained and undrained tests, but the peak stress ratio of the drained condition is slightly higher than that of the undrained condition. The shape of the η-ε_s relationship for drained and undrained conditions are significantly different. Under undrained conditions, the stress ratio has an obvious peak value, and the peak stress ratio decreases slightly with the increase of ε_s. In Figures 8b and 9b, the ε_s/η-ε_s relationships are linear under drained and undrained conditions. The slope of the straight line increases with the increase of the effective confining pressure under the drained condition, but the change of the slope is small under an undrained condition.

Wood et al. [38] used the peak generalized stress ratio to represent the characteristics of the softening curve and proposed a hyperbolic model characterized by the stress ratio and the shear strain, which reads:

$$\frac{\eta}{\eta_{\max}} = \frac{\varepsilon_s}{B + \varepsilon_s} \tag{1}$$

where B is the test constant and $\eta_{\max}$ is the peak value of the generalized stress ratio. The transformation form is as follows.

$$\frac{\varepsilon_s}{\eta} = \frac{B}{\eta_{\max}} + \frac{\varepsilon_s}{\eta_{\max}} \tag{2}$$

Our test results are consistent with the hyperbolic model proposed by Wood et al. [38]. The slope of the ε_s/η-ε_s curve increases gradually with the increase of effective confining pressure under drained conditions, indicating that softening increases gradually. The slope of the ε_s/η-ε_s curve under undrained conditions is significantly higher than that under drained conditions, indicating that the softening phenomenon is more obvious.

Figure 10 shows the variation of peak shear stress and peak friction angle with effective confining pressure under drained and undrained conditions. The black curve in the figure increases linearly, indicating that the generalized peak shear stress increases linearly with the increase of effective confining pressure under both drained and undrained conditions. However, the undrained strength is greater than the drained strength at low effective confining pressure, and the drained and undrained strength becomes the same as the effective confining pressure increases. All the purple curves show a nonlinear decreasing trend, indicating that the peak friction angle decreases nonlinearly with the increase of effective confining pressure. At low effective confining pressure, the peak friction angles of the two test conditions are quite different, but at high effective confining pressure they are close to the same.

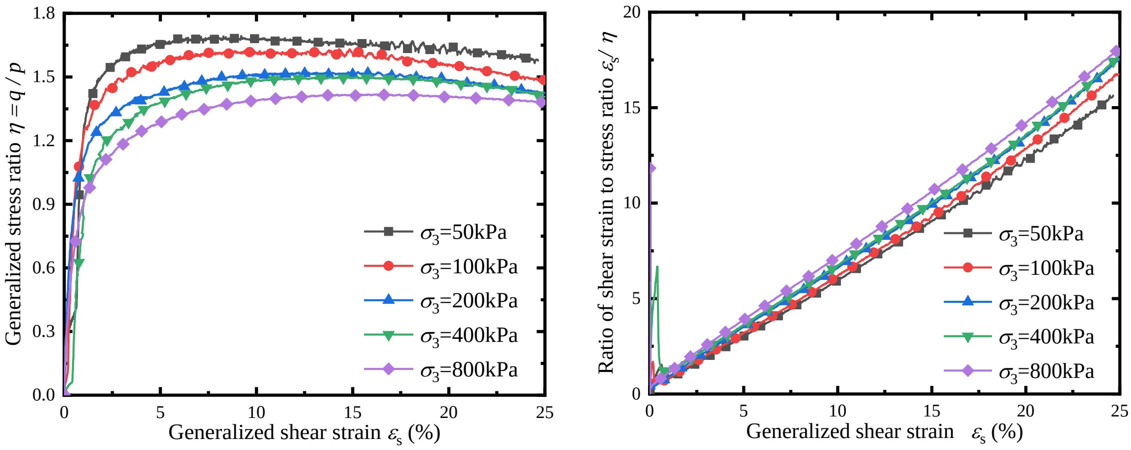

(**a**) (**b**)

Figure 8. η-ε_s relationships and ε_s/η-ε_s relationships under drained condition. (**a**) η-ε_s relationships under drained condition. (**b**) ε_s/η-ε_s relationships under drained condition.

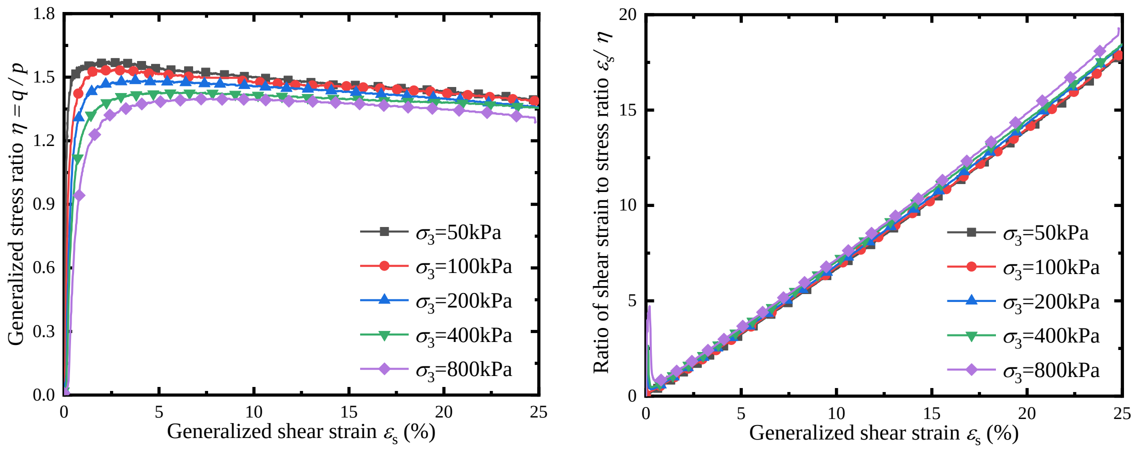

(**a**) (**b**)

Figure 9. η-ε_s relationships and ε_s/η-ε_s relationships under undrained condition. (**a**) η-ε_s relationships under undrained condition. (**b**) ε_s/η-ε_s relationships under undrained condition.

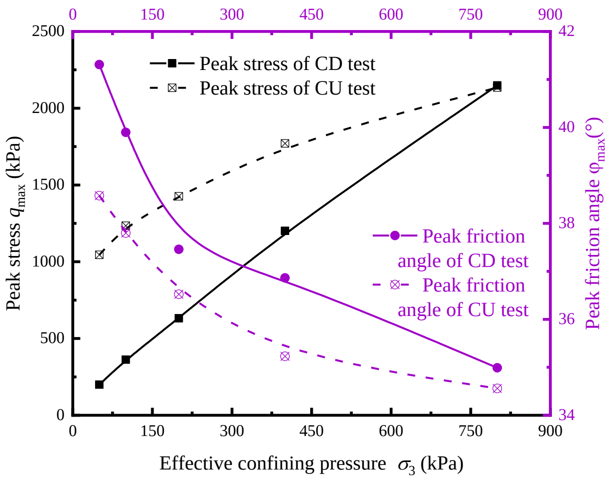

Figure 10. The relationships between q_{max}~σ_3 and φ_{max}~σ_3 under drained and undrained conditions.

3.2. State Boundary Surface

Figure 11 plots the critical state line and phase transformation line in the *p*-*q* space under drained and undrained conditions and gives the slopes of the two-state lines. The green points in Figure 11a are the phase transformation points, which are the inflection points where the void ratio changes from decrease to increase, and it is also the transformation point of volumetric change from contraction to dilation. The phase transformation point is determined according to the corresponding stress state point, as the void ratio increment is 0. Figure 11 shows that the critical state line and phase transformation line determined by the undrained triaxial test are slightly lower than those determined by the drained triaxial test, due to the change of pore pressure and shear rate, and the variation range is less than 5%. The test results show that the aeolian sand has a unified critical state line and phase transformation line.

The critical state line and phase transformation line of aeolian sand in the *p*-*q* space can be expressed linearly by the following equations:

$$q = M_{\mathrm{CSL1}}p \tag{3}$$

$$q = M_{\mathrm{PTL1}}p \tag{4}$$

where M_{CSL1} and M_{PTL1} are the slopes of the critical state line and the phase transformation line in *p*-*q* space, respectively.

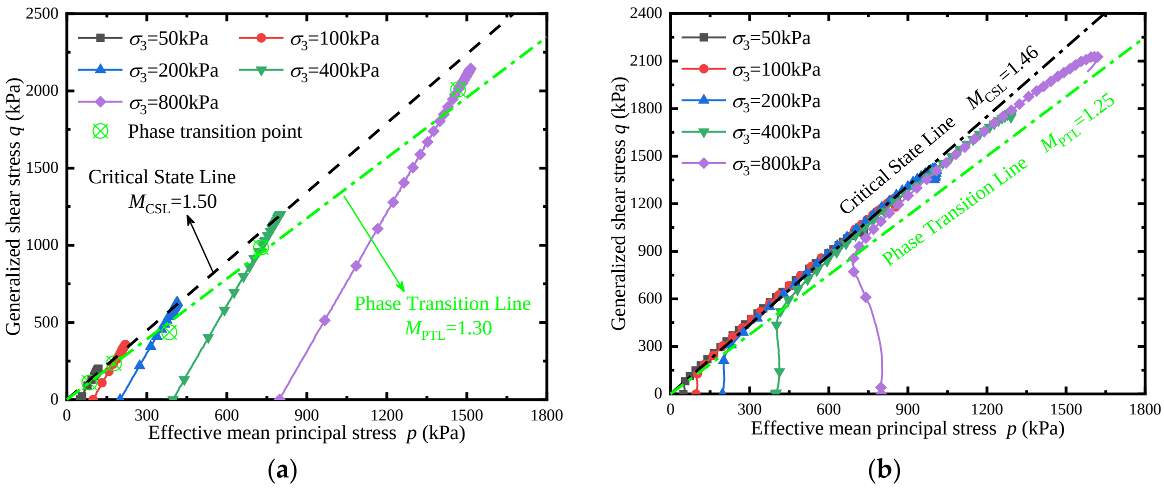

Figure 11. Effective stress path for drained and undrained test. (**a**) Effective stress path for drained test. (**b**) Effective stress path for undrained test.

The information in Figure 12 shows the critical state line, phase transformation line and normal consolidation line under drained conditions, which can be represented by linear relations. At the same effective confining pressure, with the increase of ln *p*, the void ratio decreases first and then increases rapidly to the critical state (compared to the consolidated void ratio). At different effective confining pressures, with the increase of effective confining pressure and ln *p*, the decreased degree of void ratio increases gradually compared with the consolidated void ratio. While the effective confining pressure is greater than 800 kPa, the void ratio is always smaller than the consolidation void ratio, and the aeolian sand undergoes only contractive deformation under this condition. The studies of Verdugo and Ishihara [39], Riemer and Seed [40] show that the critical state characteristics of cohesionless soil are significantly different from those of clay, and the critical state line is no longer unique in the ln *p*-*e* space, due to the anisotropy of the soil. In this study, the specimen adopts the same specimen preparation method and is sheared under triaxial conditions, so the critical state lines, phase transformation lines and normal consolidation lines of aeolian sand in *e*-ln *p* space can be expressed by linear equations as expressed by Equations (5)–(7), respectively.

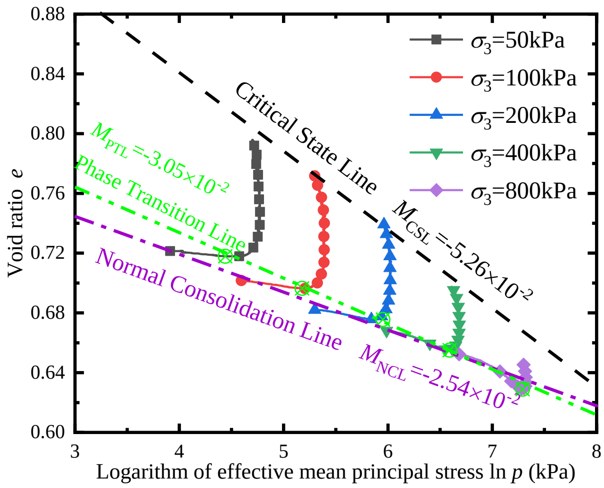

Figure 12. *e*-ln *p* relationships under drained conditions.

$$e_{\mathrm{CSL}} = M_{\mathrm{CSL2}} \ln p + e_{\mathrm{C}} \tag{5}$$

$$e_{\mathrm{PTL}} = M_{\mathrm{PTL2}} \ln p + e_{\mathrm{P}} \tag{6}$$

$$e_{\mathrm{NCL}} = M_{\mathrm{NCL}} \ln p + e_{\mathrm{N}} \tag{7}$$

where e_{CSL2}, e_{PTL2} and e_{NCL} are the void ratios corresponding to the critical state line, the phase transformation line and the normal consolidation line at any p, respectively. M_{CSL2}, M_{PTL2} and M_{NCL} are the slopes of the critical state line, phase transformation line and normal consolidation line in ln p-e space, respectively. e_{C},e_{P} and e_{N} are the void ratios corresponding to the critical state line, phase transformation line and normal consolidation line at p = 1 kPa, respectively.

Figure 13 shows the e-q relationships of aeolian sand under drained conditions. The shape characteristics of the critical state line and the phase transformation line in the e-q space are exponential. Moreover, as q increases, the void ratio decreases compared with the consolidated void ratio, and the specimen contracts. At low and medium effective confining pressure, the void ratio increases rapidly to a critical state after reaching the phase transformation point. At high effective confining pressures, the void ratio increases and q decreases, and the specimen show strain softening behaviours. At low effective confining pressures, and the dilatation characteristics are significant. The higher the effective confining pressure, the greater the peak shear stress. The critical state lines and phase transformation lines in e-q space are nonlinear. The critical state line and phase transformation line can be used to predict the development trend of voids under different test conditions. According to Equations (3) and (5), the critical state line in e-q space can be expressed as follows:

$$q = M_{\mathrm{CSL1}} p = M_{\mathrm{CSL1}} \exp \frac{e_{\mathrm{CSL}} - e_{\mathrm{C}}}{M_{\mathrm{CSL2}}} \tag{8}$$

Based on Equations (4) and (6), the phase transformation line in e-q space can be expressed as follows:

$$q = M_{\mathrm{PTL1}} p = M_{\mathrm{PTL1}} \exp \frac{e_{\mathrm{PTL}} - e_{\mathrm{P}}}{M_{\mathrm{PTL2}}} \tag{9}$$

Figure 14 shows the critical state characteristic curve of aeolian sand in e-p-q space. The three-dimensional surface composed of e, p and q is the state boundary surface or Roscoe surface. The curve connected by the transformation points where the void ratio first decreases and then increases at different stress states is defined as the phase transformation state line, which reflects the state transformation from contraction to dilation. While the granular material is sheared to failure, the curve composed of the effective stress path, void ratio and average effective stress is defined as the critical state line. The three-dimensional critical state line can be expressed in Equations (5) and (7), and reads:

$$\begin{cases} e_{\mathrm{CSL}} = M_{\mathrm{CSL2}} \ln p + e_{\mathrm{C}} \\ q = M_{\mathrm{CSL1}} \exp \frac{e_{\mathrm{CSL}} - e_{\mathrm{C}}}{M_{\mathrm{CSL2}}} \end{cases} \tag{10}$$

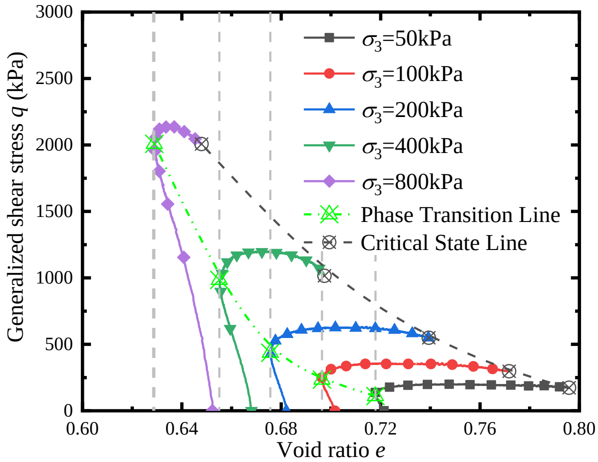

Figure 13. *e*-*q* relationships under drained conditions.

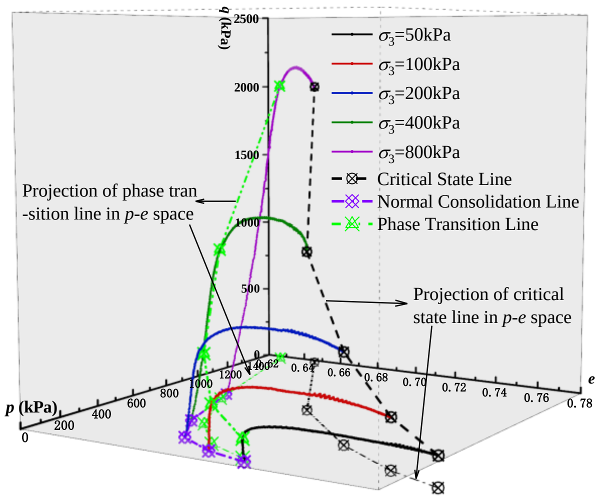

Figure 14. State boundary surface in three-dimensional space.

The three-dimensional phase transformation line can be expressed in Equations (6) and (8), and reads:

$$\begin{cases} e_{\mathrm{PTL}} = M_{\mathrm{PTL2}} \ln p + e_{\mathrm{P}} \\ q = M_{\mathrm{PTL1}} \exp \frac{e_{\mathrm{PTL}} - e_{\mathrm{P}}}{M_{\mathrm{PTL2}}} \end{cases} \tag{11}$$

The test results take into account the dilatancy characteristics for the establishment of the state boundary surface, so the state boundary surface is quite different from that of remodelled clay proposed by Roscoe [1]. The state boundary surface describes the unique relationship among the stress state, strength and void ratio of aeolian sand. The spatial critical state line and phase transformation line shown in Figure 14 and their descriptive Equations (9) and (10) can better describe and predict the quantitative relationship between stress state characteristics and volume state characteristics in the three-dimensional space.

4. Conclusions

In this paper, the state boundary surface and deformation and failure characteristics of aeolian sand in the Tengger Desert, China are studied through a series of drained and undrained triaxial tests. The following conclusions can be drawn from this study:

(1) The generalized peak shear stress of aeolian sand increases linearly with the increase of effective confining pressure under drained and undrained conditions; the undrained strength is greater than the drained strength at low effective confining pressure, and the strength is close to the same with the increase of effective confining pressure. The peak friction angle decreases nonlinearly with the increase of effective confining pressure. The peak friction angle of the two test conditions is quite different at low effective confining pressure and is close to the same at high effective confining pressure.

(2) At low and medium effective confining pressures, the dilatancy is obvious. With the increase of effective confining pressures, the dilatancy develops to contraction. At high effective confining pressures, it only contracts. The development of pore pressure under undrained conditions also reflects a similar law.

(3) The medium-density specimen of aeolian sand obtained by the multiple sieving pluviation method has strong initial anisotropy. With the increase of effective confining pressure, the effect of initial anisotropy gradually weakens. While the effective confining pressure is 800 kPa, the initial anisotropy has almost no effect on the deformation characteristics. The initial anisotropy characteristics of the undrained test are not obvious, and the relationships between axial strain and radial strain always satisfy the relationship $\varepsilon_1 = -2\varepsilon_3$.

(4) The three-dimensional state boundary surface of aeolian sand considering dilatancy is quite different from that of remoulded clay. The study of the state boundary surface and the determination of critical state line and phase transformation line equations in three-dimensional space describe the unique state relationship formed by the generalized normal stress, shear stress and void ratio accurately, which can predict the quantitative relationship between stress state and volumetric state reasonably. The state boundary parameters can provide the basis for the establishment of the constitutive model of aeolian sand and provide basic test support for the geotechnical design, construction and maintenance of foundations, roadbeds and another foundation engineering in desert areas.

Author Contributions: Conceptualization, Z.M. and X.L.; methodology, X.L.; validation, Z.M., X.L.; formal analysis, X.L.; investigation, Z.M.; resources, X.L.; data curation, Z.M.; writing—original draft preparation, Z.M.; writing—review and editing, Z.M. and X.L.; visualization, Z.M.; supervision, X.L.; funding acquisition, X.L. All authors have read and agreed to the published version of the manuscript.

Funding: This work was financially supported by the Projects for Leading Talents of Science and Technology Innovation of Ningxia (No. KJT2019001), the National Natural Science Foundation of China (No. 12162028), and the innovation team for multi-scale mechanics and its engineering applications of Ningxia Hui Autonomous Region (2021), and these supports are gratefully acknowledged.

Institutional Review Board Statement: Not applicable.

Informed Consent Statement: Informed consent was obtained from all subjects involved in the study.

Data Availability Statement: The data used to support the findings of this study are available from the corresponding author upon request.

Conflicts of Interest: The authors declare no conflict of interest.

References

1. Schofield, A.N.; Wroth, P. *Critical State Soil Mechanics*; McGraw-Hill: London, UK, 1968; Volume 310.
2. Li, J.; Zhang, J.; Yang, X.; Zhang, A.; Yu, M. Carlo simulations of deformation behaviour of unbound granular materials based on a real aggregate library. *Int. J. Pavement. Eng.* **2023**. [CrossRef]
3. Fan, H.; Zhang, J.; Zheng, J. Dynamic response of a multi-layered pavement structure with subgrade modulus varying with depth subjected to a moving load. *Soil. Dyn. Earthq. Eng.* **2022**, *160*, 107358. [CrossRef]
4. Wang, X.Y.; Liu, M.H.; Liu, X.; Jia, S.Y.; Xu, Z. Study on mechanical properties and carbon emissions of desert sand and machine—Made sand concrete. *China Civ. Eng. J.* **2022**, *55*, 23–30. [CrossRef]
5. Wang, H.; Huang, X.; Xie, B. Strength and deformation properties of structural lightweight concrete under true tri-axial compression. *Case Stud. Constr. Mater.* **2019**, *11*, e00269. [CrossRef]
6. Wang, Y.H.; Chu, Q.; Han, Q. Filling effect of kubuqi aeolian sand on different classifications of river sand. *J. Build. Mater.* **2021**, *24*, 191–198.
7. Dong, Z.B.; Cui, X.J. Grain-size characteristics of transverse dune during different developmental stages in the southeastern edge of the Tengger Desert. *J. Desert Res.* **2015**, *35*, 129–135. [CrossRef]
8. Liu, Z.Y.; Jin, H.L.; Liu, B.; Xue, W.P. Desert evolution during the mid holocene reflected by grain-size variation of aeolian sand and paleosoil sequence records from Mu Us sandy land. *J. Desert Res.* **2019**, *39*, 88–96.
9. Ning, K.; Li, Z.L.; Wang, N.A.; Sun, J.W.; Shao, W.W. Spatial characteristics of grain size and its environmental implication in the Badain Jaran Desert. *J. Desert Res.* **2013**, *33*, 642–648.
10. Guo, F.; Sun, D.H.; Wang, F.; Li, Z.J.; Li, B.F. Grain-size distribution pattern of the depositional sequence in central Badain Jaran Desert andits genetic interpretation. *Mar. Geol. Quat. Geol.* **2014**, *34*, 165–173.
11. Zhang, D.S.; Tian, L.H.; Lu, R.J.; Tang, Q.L.; Shi, H. Grain-size features of aeolian deposits in the eastern shore of Qinghai lake. *Arid. Land Geogr.* **2013**, *36*, 203–211.
12. Yuan, Y.Q.; Wang, X.C. Experimental research on compaction characteristics of aeolian sand. *Chin. J. Geotech. Eng.* **2007**, *29*, 360–365. [CrossRef]
13. Li, Z.Y.; Cao, Y.W.; Liang, N.X.; Mei, Y.J. Compaction mechanism of aeolian sand. *China J. Highw. Transp.* **2006**, *19*, 6–11.
14. Yin, Y.Z.; Wang, Y.L. Study of Key Parameters in the Process of Aeolian Sand Compactibility. *Appl. Mech. Mater.* **2014**, 278–282. [CrossRef]
15. Du, X.L.; Yang, J.B.; Zhang, X.F. Research on relationships between shear strength index and in-situ indexes of desert sand. *Rock Soil Mech.* **2005**, *26*, 837–840. [CrossRef]
16. Yu, Y.F.; Zhang, X.F.; Jiao, Q.X.; Zhao, Y.M. Research on engineering properties of desert sands in Taklimakan Desert. *J. Desert Res.* **2007**, *27*, 362–366.
17. Yi, F.; Hong, C.; Xue, Y.Z.; Kaidi, Z. Shear strength of aeolian sand sediments. *Trans. ASABE* **2018**, *61*, 583–590. [CrossRef]
18. Zheng, M.L.; Wang, Q.Q.; Chen, W.; Gao, Y.; Zhang, S.; Zhu, L.L. Materials characteristics and shear strength of aeolian sand in different areas. *China Sci.* **2021**, *16*, 415–421.
19. Yin, Y.Z.; Wang, Y.L. Determine the Shear Strength of Aeolian Sand and Bearing Capacity. *Appl. Mech. Mater.* **2014**, *580*, 165–168. [CrossRef]
20. Li, Y.; Zhang, D.; Wu, C. Sensitivity study of the bearing capacity and pile-soil stress ratio for aeolian sand foundation treated with CFG piles. *Rev. TÉCnica De La Fac. De Ing. Univ. Del Zulia* **2017**, *39*, 124–135.
21. Deng, Y.H.; Li, X.A.; Wang, Z.J.; Song, Y.X.; Pen, J.B. Study on dynamic strength of the aeolian sand inmaowusu desert area. *Eng. Mech.* **2012**, *29*, 281–286.
22. Song, Y.X. Test Study on the Mechanical Property of the Aeolian Sand and the Bearing Capacity of the Aeolian Sand Ground of Mu Us Desert. Ph.D. Thesis, Chang'an University, Xi'an, China, 2011.
23. Liu, D.; Yang, X.; Wang, J.; Mao, Z.J. Study on Static Strength of Aeolian Sand before and after Cyclic Loading. *Appl. Mech. Mater.* **2014**, *580*, 191–194. [CrossRef]
24. Song, Y.; Zhang, X.D.; Zhang, X. Experimental study on the characteristics of weakened subgrade of aeolian soil along the Beijing-Shenyang super rail. *J. Saf. Environ.* **2014**, *14*, 69–73.
25. Liu, D.P.; Yang, X.H.; Wang, Y.W. Study on the plastic strain characteristics of aeolian sand under cyclic loading. *J. Wuhan Univ. Technol.* **2014**, *36*, 103–108.
26. Luo, J.W.; Li, X.A.; Zhao, N.; Zhou, J.; Zhao, X.K. Experimental study on dynamic characteristics of sandy loess of aeolian sand to loess transitional origin. *J. Eng. Geol.* **2016**, *24*, 915–923.
27. Bao, J.Q.; Xing, Y.M.; Liu, L. Dynamic characteristics of reinforced aeolian sands with geogrid. *Ind. Constr.* **2019**, *49*, 77–81+107.
28. Li, J.; Wang, F.; Yi, F.; Wu, F.; Liu, J.; Lin, Z. Effect of freeze-thaw cycles on triaxial strength property damage to cement improved aeolian sand (CIAS). *Materials* **2019**, *12*, 2801. [CrossRef] [PubMed]
29. Badanagki, M. Shear Strength and Stiffness of a Sahara Sand from Libya. Ph.D. Thesis, Colorado State University, Fort Collins, CO, USA, 2011.
30. Qureshi, M.U.; Chang, I.; Al-Sadarani, K. Strength and durability characteristics of biopolymer-treated desert sand. *Geomech. Eng.* **2017**, *12*, 785–801. [CrossRef]
31. Souza Júnior, P.L.; Santos Júnior, O.F.; Fontoura, T.B.; Freitas Neto, O.D. Drained and undrained behavior of an aeolian sand from Natal, Brazil. *Soils Rocks São Paulo* **2020**, *43*, 263–270. [CrossRef]

32. Wei, X.; Gao, C.; Ai, K.; Zhao, J.; Xu, L. Mechanical Interpretation of Effects of Aeolian FineSands on Coal Fly Ash in Northern Shaanxi Province, China. *Adv. Civ. Eng.* **2020**. [CrossRef]
33. Li, X.; Xu, W.; Chang, L.; Yang, W. Shear Behaviour of Aeolian Sand with Different Density and Confining Pressure. *Appl. Sci.* **2022**, *12*, 3020. [CrossRef]
34. Li, X.; Ma, Z.; Lu, W.; Wang, Y. True-Triaxial Drained Test of Tengger Desert Sand. *Adv. Civ. Eng.* **2020**, *2020*, 8851165. [CrossRef]
35. Li, X.F.; Lu, W.N.; Ma, Z.G.; Tuo, N. The Undrained Characteristics of Tengger Desert Sand from True Triaxial Testing. *Adv. Civ. Eng.* **2021**, *2021*, 6320397. [CrossRef]
36. Li, J.S.; Zhang, Y.Z. Undrained monotonic and dynamic triaxial properties of the aeolian sand. In *IOP Conference Series: Earth and Environmental Science*; IOP Publishing: Bristol, UK, 2019; Volume 242, p. 062010.
37. Skempton, A. Effective stress in soils, concrete and rocks. *Sel. Pap. Soil Mech.* **1984**, *1032*, 4–16.
38. Wood, D.M.; Belkheir, K. Strain softening and state parameter for sand modelling. *GÉOtechnique* **1994**, *44*, 335–339. [CrossRef]
39. Verdugo, R.; Ishihara, K. The steady state of sandy soils. *Soils Found.* **1996**, *36*, 81–91. [CrossRef] [PubMed]
40. Riemer, M.F.; Seed, R.B. Factors affecting apparent position of steady-state line. *J. Geotech. Geoenvironmental Eng.* **1997**, *123*, 281–288. [CrossRef]